Biomedical Optics EXPRESS

Optical mesoscopy without the scatter: broadband multispectral optoacoustic mesoscopy

Andrei Chekkoury,[1,2] Jérôme Gateau,[1,2] Wouter Driessen,[2,3] Panagiotis Symvoulidis,[1,2] Nicolas Bézière,[1,2] Annette Feuchtinger,[4] Axel Walch,[4] and Vasilis Ntziachristos[1,2,*]

[1]*Chair for Biologial Imaging, Technische Universität München (TUM), Ismaningerstr. 22, 81675, Munich, Germany*
[2]*Institute for Biological and Medical Imaging (IBMI), Helmholtz Zentrum München, Ingolstädter Landstraße 1, 85764, Neuherberg, Germany*
[3]*iThera Medical, GmbH, Zielstattstraße 13, 81379, Munich, Germany*
[4]*Research Unit of Analytical Pathology, Institute of Pathology, Helmholtz ZentrumMünchen, IngolstädterLandstraße 1, 85764 Neuherberg, Germany*
[*]*v.ntziachristos@tum.de*

Abstract: Optical mesoscopy extends the capabilities of biological visualization beyond the limited penetration depth achieved by microscopy. However, imaging of opaque organisms or tissues larger than a few hundred micrometers requires invasive tissue sectioning or chemical treatment of the specimen for clearing photon scattering, an invasive process that is regardless limited with depth. We developed previously unreported broadband optoacoustic mesoscopy as a tomographic modality to enable imaging of optical contrast through several millimeters of tissue, without the need for chemical treatment of tissues. We show that the unique combination of three-dimensional projections over a broad 500 kHz–40 MHz frequency range combined with multi-wavelength illumination is necessary to render broadband multispectral optoacoustic mesoscopy (2B-MSOM) superior to previous optical or optoacoustic mesoscopy implementations.

OCIS codes: (110.5120) Photoacoustic imaging; (110.5125) Photoacoustics; (110.6955) Tomographic imaging; (110.4234) Multispectral and hyperspectral imaging; (330.6180) Spectral discrimination.

References and links

1. V. Ntziachristos, "Going deeper than microscopy: the optical imaging frontier in biology," Nat. Methods **7**(8), 603–614 (2010).
2. C. Vinegoni, C. Pitsouli, D. Razansky, N. Perrimon, and V. Ntziachristos, "In vivo imaging of Drosophila melanogaster pupae with mesoscopic fluorescence tomography," Nat. Methods **5**(1), 45–47 (2007).
3. H. U. Dodt, U. Leischner, A. Schierloh, N. Jährling, C. P. Mauch, K. Deininger, J. M. Deussing, M. Eder, W. Zieglgänsberger, and K. Becker, "Ultramicroscopy: three-dimensional visualization of neuronal networks in the whole mouse brain," Nat. Methods **4**(4), 331–336 (2007).
4. J. Sharpe, U. Ahlgren, P. Perry, B. Hill, A. Ross, J. Hecksher-Sørensen, R. Baldock, and D. Davidson, "Optical projection tomography as a tool for 3D microscopy and gene expression studies," Science **296**(5567), 541–545 (2002).
5. W. Kriz and H. Koepsell, "The structural organization of the mouse kidney," Z. Anat. Entwicklungsgesch. **144**(2), 137–163 (1974).
6. P. Treuting and S. M. Dintzis, *Comparative anatomy and histology: A mouse and human atlas* (Academic Press, 2011).
7. T. Alanentalo, A. Asayesh, H. Morrison, C. E. Lorén, D. Holmberg, J. Sharpe, and U. Ahlgren, "Tomographic molecular imaging and 3D quantification within adult mouse organs," Nat. Methods **4**(1), 31–33 (2007).
8. J. Huisken, J. Swoger, F. Del Bene, J. Wittbrodt, and E. H. Stelzer, "Optical sectioning deep inside live embryos by selective plane illumination microscopy," Science **305**(5686), 1007–1009 (2004).
9. L. V. Wang and S. Hu, "Photoacoustic tomography: in vivo imaging from organelles to organs," Science **335**(6075), 1458–1462 (2012).
10. D. Razansky, M. Distel, C. Vinegoni, R. Ma, N. Perrimon, R. W. Köster, and V. Ntziachristos, "Multispectral opto-acoustic tomography of deep-seated fluorescent proteins in vivo," Nat. Photonics **3**(7), 412–417 (2009).

#237714 Received 13 Apr 2015; revised 6 Jun 2015; accepted 9 Jun 2015; published 31 Jul 2015

11. J. Gateau, A. Chekkoury, and V. Ntziachristos, "High-resolution optoacoustic mesoscopy with a 24 MHz multidetector translate-rotate scanner," J. Biomed. Opt. **18**(10), 106005 (2013).
12. J. Gateau, A. Chekkoury, and V. Ntziachristos, "Ultra-wideband three-dimensional optoacoustic tomography," Opt. Lett. **38**(22), 4671–4674 (2013).
13. T. Lasser, A. Soubret, J. Ripoll, and V. Ntziachristos, "Surface reconstruction for free-space 360 degrees fluorescence molecular tomography and the effects of animal motion," IEEE Trans. Med. Imaging **27**(2), 188–194 (2008).
14. S. Michau, P. Mauchamp, and L. Dufait, "Piezocomposite 30MHz linear array for medical imaging: design challenges and performances evaluation of a 128 elements array," in *Ultrasonics Symposium, 2004 IEEE*, (IEEE, 2004), 898–901.
15. T. Jetzfellner, A. Rosenthal, A. Buehler, A. Dima, K.-H. Englmeier, V. Ntziachristos, and D. Razansky, "Optoacoustic tomography with varying illumination and non-uniform detection patterns," J. Opt. Soc. Am. A **27**(11), 2488–2495 (2010).
16. J. Gateau, M. A. A. Caballero, A. Dima, and V. Ntziachristos, "Three-dimensional optoacoustic tomography using a conventional ultrasound linear detector array: Whole-body tomographic system for small animals," Med. Phys. **40**(1), 013302 (2013).
17. R. Ma, A. Taruttis, V. Ntziachristos, and D. Razansky, "Multispectral optoacoustic tomography (MSOT) scanner for whole-body small animal imaging," Opt. Express **17**(24), 21414–21426 (2009).
18. E. Herzog, A. Taruttis, N. Beziere, A. A. Lutich, D. Razansky, and V. Ntziachristos, "Optical Imaging of Cancer Heterogeneity with Multispectral Optoacoustic Tomography," Radiology **263**(2), 461–468 (2012).
19. M. V. Marshall, D. Draney, E. M. Sevick-Muraca, and D. M. Olive, "Single-dose intravenous toxicity study of IRDye 800CW in Sprague-Dawley rats," Mol. Imaging Biol. **12**(6), 583–594 (2010).
20. A. Taruttis, S. Morscher, N. C. Burton, D. Razansky, and V. Ntziachristos, "Fast Multispectral Optoacoustic Tomography (MSOT) for Dynamic Imaging of Pharmacokinetics and Biodistribution in Multiple Organs," PLoS ONE **7**(1), e30491 (2012).
21. A. Taruttis, E. Herzog, D. Razansky, and V. Ntziachristos, "Real-time imaging of cardiovascular dynamics and circulating gold nanorods with multispectral optoacoustic tomography," Opt. Express **18**(19), 19592–19602 (2010).
22. B. Ergin, S. Meding, R. Langer, M. Kap, C. Viertler, C. Schott, U. Ferch, P. Riegman, K. Zatloukal, A. Walch, and K. F. Becker, "Proteomic analysis of PAXgene-fixed tissues," J. Proteome Res. **9**(10), 5188–5196 (2010).
23. M. Dobosz, V. Ntziachristos, W. Scheuer, and S. Strobel, "Multispectral Fluorescence Ultramicroscopy: Three-Dimensional Visualization and Automatic Quantification of Tumor Morphology, Drug Penetration, and Antiangiogenic Treatment Response," Neoplasia **16**(1), 1–13 (2014).
24. A. Sarantopoulos, G. Themelis, and V. Ntziachristos, "Imaging the bio-distribution of fluorescent probes using multispectral epi-illumination cryoslicing imaging," Mol. Imaging Biol. **13**(5), 874–885 (2011).
25. P. Beard, "Biomedical photoacoustic imaging," Interface Focus **1**(4), 602–631 (2011).
26. G. Ku, X. Wang, G. Stoica, and L. V. Wang, "Multiple-bandwidth photoacoustic tomography," Phys. Med. Biol. **49**(7), 1329–1338 (2004).
27. E. Zhang, J. Laufer, and P. Beard, "Backward-mode multiwavelength photoacoustic scanner using a planar Fabry-Perot polymer film ultrasound sensor for high-resolution three-dimensional imaging of biological tissues," Appl. Opt. **47**(4), 561–577 (2008).
28. A. Rosenthal, S. Kellnberger, D. Bozhko, A. Chekkoury, M. Omar, D. Razansky, and V. Ntziachristos, "Sensitive interferometric detection of ultrasound for minimally invasive clinical imaging applications," Laser Photon. Rev. **8**(3), 450–457 (2014).
29. M. Omar, J. Gateau, and V. Ntziachristos, "Raster-scan optoacoustic mesoscopy in the 25-125 MHz range."
30. J. Laufer, E. Zhang, G. Raivich, and P. Beard, "Three-dimensional noninvasive imaging of the vasculature in the mouse brain using a high resolution photoacoustic scanner," Appl. Opt. **48**(10), D299–D306 (2009).
31. H. F. Zhang, K. Maslov, G. Stoica, and L. V. Wang, "Functional photoacoustic microscopy for high-resolution and noninvasive in vivo imaging," Nat. Biotechnol. **24**(7), 848–851 (2006).
32. S. Tzoumas, N. Deliolanis, S. Morscher, and V. Ntziachristos, "Unmixing Molecular Agents From Absorbing Tissue in Multispectral Optoacoustic Tomography," IEEE Trans. Med. Imaging **33**(1), 48–60 (2014).
33. M. A. Araque Caballero, J. Gateau, X.-L. Dean-Ben, and V. Ntziachristos, "Model-based optoacoustic image reconstruction of large three-dimensional tomographic datasets acquired with an array of directional detectors," IEEE Trans. Med. Imaging **33**(2), 433–443 (2014).
34. R. Mañalich, L. Reyes, M. Herrera, C. Melendi, and I. Fundora, "Relationship between weight at birth and the number and size of renal glomeruli in humans: a histomorphometric study," Kidney Int. **58**(2), 770–773 (2000).
35. F. J. Sampaio and A. H. Aragao, "Anatomical relationship between the intrarenal arteries and the kidney collecting system," J. Urol. **143**(4), 679–681 (1990).
36. Y. Liu, "Renal fibrosis: new insights into the pathogenesis and therapeutics," Kidney Int. **69**(2), 213–217 (2006).
37. M. Feuerstein, H. Heibel, J. Gardiazabal, N. Navab, and M. Groher, "Reconstruction of 3-D histology images by simultaneous deformable registration," in *Medical Image Computing and Computer-Assisted Intervention–MICCAI 2011* (Springer, 2011), pp. 582–589.

1. Introduction

Optical mesoscopy generally refers to optical imaging achieved at depths or tissue sizes that go beyond the depths reached by multi-photon microscopy, i.e. ~0.5 mm of scattering tissue

#237714 Received 13 Apr 2015; revised 6 Jun 2015; accepted 9 Jun 2015; published 31 Jul 2015

[1]. On the opposite end, mesoscopy is bounded by optical macroscopy, which generally addresses imaging of entire animals or even humans.

Mesoscopy has been receiving significant attention in the past decade, as investigations of functional genomics shifted attention to studying entire organisms and organs [2]. Originally studied by histology, fish, insects, small animal embryos and extremities or implanted subcutaneous tumors have been more recently imaged by selective plane illumination microscopy (SPIM) [3] or Optical Projection Tomography (OPT) [4]. The rationale of mesoscopic studies lies in imaging volumes that are larger than the ones sampled by microscopy, so that a more complete picture of biological phenomena is obtained. Optical mesoscopy further improves upon the labor-intensive process of histological analysis, the latter performed on fixed tissues by imaging individual tissue slices [5, 6], a process that may alter morphological characteristics.

These advantages have led to several applications. Targeting anatomical and functional imaging, OPT has been used to obtain high-resolution 3D images of embryonic structures after tissue-specific labeling by certain antibodies. Insights into developmental biology and experimental genetics were gained in studying phases of the developing nervous system or rapid mapping of the tissue distribution of RNA and protein expression [4]. A correlation between the total islet β-cell volume in animal pancreata and the onset of type-1 diabetes was established [7]. SPIM has visualized entire chemically treated mouse brains and detected single GFP-labeled neurons within dendritic trees in isolated hippocampi [3]. SPIM has also been able to offer in-vivo fast imaging capabilities [8] by dynamically visualizing GFP labeled somatic and smooth muscles and the myocardium of fish embryos, at 6 μm resolution as deep as 500 μm inside transparent animals.

Nevertheless, optical mesoscopy today comes with limitations. OPT and SPIM can yield sub-10 micrometer resolution in volumetric imaging but only of transparent specimen, typically no more than 1 mm in diameter. Scattering compromises the performance of volumetric optical imaging as it blurs the photon trajectories and leads to resolution loss within a few tens of micrometers of photon propagation in scattering tissue. Imaging larger specimen requires chemical treatment of tissue [7] with chemicals allowed to diffuse into tissue in order to offer clearing from photon scattering and render the tissues transparent. Alternatively, methods that model the photon propagation to yield improved performance with opaque specimen have been considered [2], yielding improved imaging ability compared to in-vivo OPT imaging. Ultimately however, this method is also affected by scattering and increasing specimen size effectively reducing the resolution achieved.

Optoacoustic imaging has been considered for high-resolution imaging that is less sensitive to photon scattering [1, 9]. Compared to raster scan approaches (ref [9].), we have shown that optoacoustic mesoscopy implemented in tomographic mode can yield superior imaging performance, providing an isotropic in-plane resolution through volumetric specimen [10]. Tomographic Optoacoustic Mesoscopy (TOM) employs sampling of ultrasonic waves at multiple angles (projections) around the object imaged [11, 12] and reconstructs the origin of the sound waves within the sample; the sound generated in response to the absorption of photon-intensity gradients (typically photon pulses) due to thermo-elastic expansion. The reconstruction of the sound origin yields images characteristic of optical absorption at the wavelength of emission. However, while optoacoustic methods have been shown to resolve the vascular system of the object imaged in great detail (i.e. high frequency components) [9], it is currently unknown whether this technique is appropriate for retrieving more elaborate patterns of tissues or extrinsic agents in mesoscopic samples.

To develop a modality that goes beyond the limitations of state-of-the-art optical and optoacoustic methods, we developed herein broad-band (2B) multispectral optoacoustic mesoscopy (MSOM) based on the TOM principle. 2B-MSOM is a previously unreported modality that offers the unique ability to collect three types of frequencies: spatial, optical (spectrum) and ultrasonic:

#237714 Received 13 Apr 2015; revised 6 Jun 2015; accepted 9 Jun 2015; published 31 Jul 2015

- Data rich in optical frequencies (wavelengths) were implemented using fast-wavelength scanning laser sources that permit tomographic MSOM to resolve specific endogenous and exogenous contrast from tissues in analogy to fluorescence employed in OPT and SPIM.
- Data rich in ultrasonic frequency were enabled using a dual ultrasonic detector array approach (Fig. 1), which allowed collection of ultrasonic frequencies from 500 kHz to 40 MHz using two overlapping detector bands at 500 kHz to 12 MHz and 2 MHz to 40 MHz This dual array approach is suited not only for high-resolution imaging due to the high frequency component but also the visualization of elaborate lower-frequency background structures present in scattering specimen with sizes of several millimeters, another feature not previously demonstrated.
- Finally the three-dimensional arrangement of 2B detectors enables an unmatched ability to collect spatial frequencies at multiple projections that lead to accurate three-dimensional imaging.

The goal of this development was to investigate whether this unique five-dimensional data set of rich spatial-optical-ultrasound frequency content collected could lead to a modality that in analogy to optical mesoscopy could resolve optical labels in highly opaque media but without the need to chemically clear the specimen imaged. Similarly to the progress seen in fluorescence molecular tomography [13], it was expected that the availability of wide-angle tomographic projections could lead to high quality and isotropic in-plane resolution imaging. However the relative imaging characteristics of MSOM versus SPIM were not known, in particular as they relate to resolving not only fluorochromes but also photo-absorbing nanoparticles and the underlying tissue anatomy using label-free, intrinsic contrast. It was hypothesized that the complementary information resulted from the two different recorded bandwidths of the detectors used in this study, would prove essential in gaining a better understanding of the underlining processes in the sample under investigation. It was expected that the availability of a broadband ultrasound frequency and enhanced sensitivity over a defined frequency band, could improve upon the limitations of narrow band optoacoustic mesoscopy and reveal not only the vascular pattern common to optoacoustic methods [9] but also more generally the lower frequency anatomical appearance of organs and structures that are not typically seen by the state-of-the-art optoacoustic methods. We further hypothesized that such performance would be necessary for identifying elaborate distribution patterns and quantifying the amounts of dyes and particles in tissues.

2. Materials and methods

2.1 Optoacoustic experimental setup

The experimental setup used in this study is based on a translate-rotate geometry previously described [11, 12]. Figure 1(a) shows a schematic of the system. A tunable (690-900 nm) optical parametric oscillator laser (Phocus II, Opotek Inc.) was used to generate <10 ns pulses with a repetition frequency of 10 Hz. The laser beam was coupled into a silica fused-end fiber bundle (CeramOptec GmbH), consisting of 640 fibers, partitioned in 4 arms. The outputs of the fiber bundle were fixed and orientated toward the sample.

Ultrasonic detection was based on two 128-element ultrasound arrays operating in tandem: one low frequency (6 MHz center frequency, 300 μm inter-element pitch, 4 mm element height, Acuson L7, Siemens Healthcare) and one high frequency (24 MHz center frequency, an average pulse-echo −6 dB bandwidth of 60%, 70 μm inter-element pitch, 1.5 mm element height, Vermon [14]). The elements were cylindrically focused in the transverse dimension using acoustic lenses, at focal length of ~19 mm and ~7.5 mm, respectively. The optoacoustic signals detected were digitized using two custom-built 128-element analog-to-digital converter (ADC) data acquisition systems; one operating at 40 MS/s sampling rate and one at 125 MS/s sampling rate, respectively. Both data acquisition cards were operating at a 12-bit resolution over a 16 mV range.

#237714 Received 13 Apr 2015; revised 6 Jun 2015; accepted 9 Jun 2015; published 31 Jul 2015

The translate-rotate scanning geometry of the detector arrays was implemented using one rotation-motorized stage and one linear translation-motorized stage (Physik Instrumente GmbH). For this geometry, the sample and the fiber bundles were fixed, and the transducer array was moved around the sample to record the ultrasonic signals. This procedure ensures the generation of a reproducible ultrasound field, and therefore prevent from having to account for a varying illumination pattern during the reconstruction procedure [15]. The stages were placed one on top of the other, such that a rotation of the translation stage was possible (Fig. 1(b)). The scanning radius for each of the transducers, matched the focal distance of the arrays.

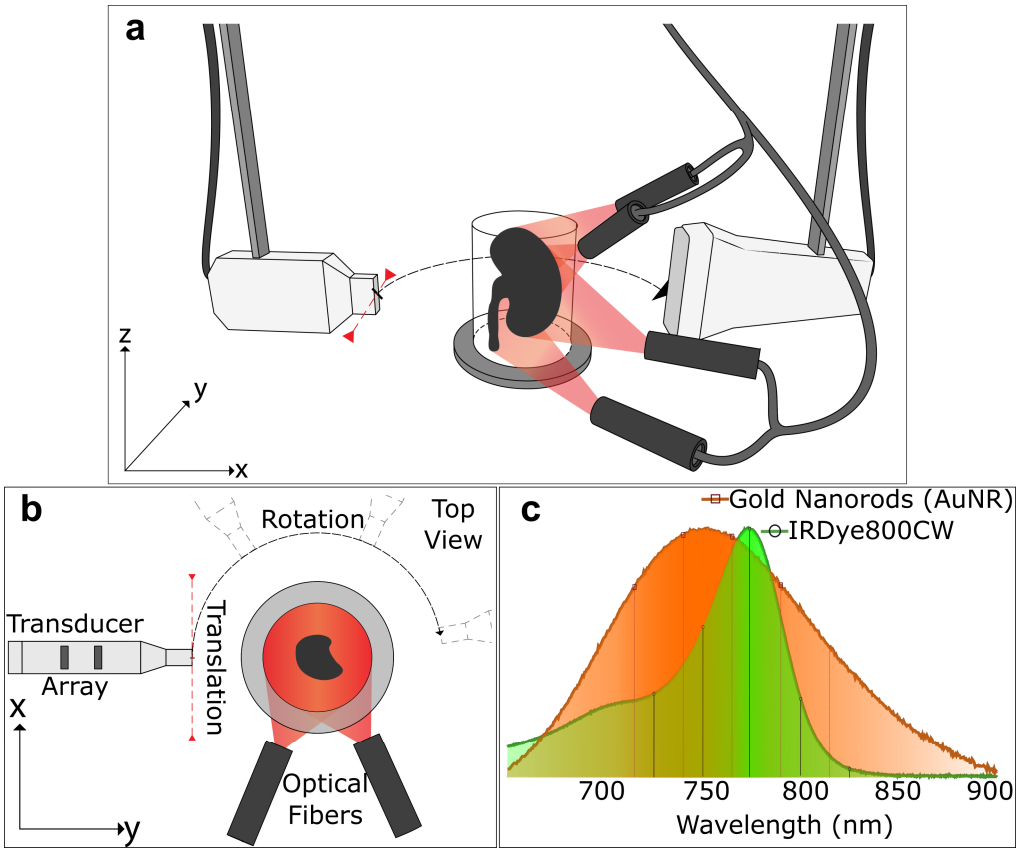

Fig. 1. Experimental set-up and absorption spectra. **a,** Perspective view: The linear transducer array is mounted on the translation stage, which is attached to a rotation stage. Both the sample and the optical fibers are fixed. The optical fibers are mounted on a supporting holder and the laser beam is directed towards the sample to obtain a homogeneous illumination. For acoustic coupling, the sample and ultrasonic transducer were immersed in water; **b,** Top view of the experimental setup; **c,** Absorption spectra of the gold nanorods (AuNR) formulation (orange) and the fluorescent agent (IRDye CW800CW) in green. The spectra were normalized by their maximum value. The vertical lines and markers indicate, for each contrast agent, the wavelengths used for optical excitation during the multispectral acquisition.

2.2 Acquisition procedure and scanning parameters

To acquire tomographic data sets, the optoacoustic imaging system performed a translate-rotate scanning motion of the detector array around the fixed sample [16]. Data sets were obtained by employing a rotation range of 178.5° and a fixed translation range for each of the transducer arrays employed (Table 1). This translation range ensured a good coverage of the sample in planes transversal to the detection probe (perpendicular to the z-axis) and enabled to obtain a homogeneous resolution over the covered scanning area [12, 16]. The scanner

#237714 Received 13 Apr 2015; revised 6 Jun 2015; accepted 9 Jun 2015; published 31 Jul 2015

allowed imaging biological samples contained in a cylinder of 10 mm diameter and 10 mm height. A continuous data acquisition procedure was employed for reducing the acquisition time compared to a stepped acquisition procedure [11, 17]. The laser was run continuously at 10Hz and signals were acquired for each laser pulse, throughout a continuous motion of the detector array. During the acquisition, the rotation and the translation stages were moved with a constant velocity, pre-determined to account for the pulse repetition rate of the laser. With this scanning parameters, the system achieved an in-plane resolution of 30 μm and 110 μm in elevation using the high-frequency transducer [11]; and 130 μm in plane resolution and 330 μm in elevation using the low-frequency array [16]. The continuous data acquisition procedure allowed performing tomographic acquisitions of the same sample at different wavelengths and with the two arrays within a reasonable time frame (Table 1). Therefore, freshly excised biological sample could be used without requirement of fixation of the tissue for preservation.

Table 1. Summary of scanning parameters

Center frequency of the array	6 MHz	24 MHz
Total number of measurement positions	2700	9060
Rotation range (°)	178.5	
Translation Range (mm)	11	9
Translation speed of the linear stage (mm/s)	4.95	1.18
Rotation speed of the rotation stage (°/s)	0.66	0.19
Acquisition time per wavelength (min)	4.5	15.1

2.3 Contrast agents

In this study, we imaged the clearance pattern of two agents: one nanoparticle formulation and one fluorescence organic dye. The first agent used was methylated gold nanorods - AuNR (Nanopartz Inc.) - a contrast agent known to stay in the blood flow for long periods of time before being hepatically excreted [18]. The second agent, a fluorochrome, was IRDye ® 800CW carboxylate (Li-Cor), a near-infrared dye, water soluble, known to be rapidly excreted by the kidneys [19].

Both injected agents had a peak optical absorption in the near-infrared wavelength range (Fig. 1(c)) and previous studies have proven their suitability for optoacoustic imaging [20, 21]. The absorbance spectrum of the dyes was recorded using a spectrometer (VIS-NIR; Ocean Optics) prior to injection. Because the contrast agents were expected in structures with various sizes within the kidney, all the samples were systematically scanned using both ultrasound transducers. Optical excitation at different wavelengths (Fig. 1(c)) was used to enable multispectral decomposition. Based on the measured spectra and on previous studies [18, 20, 21] using these contrast agents for optoacoustic imaging, a series of wavelengths on both sides of the peak absorption wavelength were selected in the following sequence: for AuNR – 715nm, 740nm, 765nm, 790nm, 815nm; for IRDye – 725nm, 750nm, 774nm, 800nm, 825nm

2.4 Sample preparation for optoacoustic imaging procedures

Aqueous solutions of contrast agents were injected intravenously into the tail vein of two CD1® mice (Charles River Laboratories). All animal experiments were carried out as approved by the district government of upper Bavaria.

The first animal (mouse *#1*) received an injection of 50 μL conjugated gold nanoparticles, at a concentration of 6e10 particles/μL. The second animal (mouse *#2*) was injected with 20 nmol of IRDye 800CW diluted in a total volume of 100 μl saline, achieving final blood concentration of approximately 10 μM.

All animals were sacrificed 15 minutes after the injection. Ten minutes after the animal's euthanasia the kidneys were excised and embedded in a supporting turbid agar gel in a

#237714 Received 13 Apr 2015; revised 6 Jun 2015; accepted 9 Jun 2015; published 31 Jul 2015

cylindrical mold (12 mm in diameter and 3.5 cm in height). The agar gel was made by mixing 1.6% w/m agar gel (Agar for microbiology, Fluka analytical) with 0.8% v/v Intralipid 20% (Sigma).

2.5 Image reconstruction and spectral unmixing

Raw optoacoustic data collected were first treated with a digital band-pass filtering (Butterworth, 3rd order), according to the bandwidth specification of the detector used: between 500 kHz and 12 MHz for the low-frequency array, and between 2 MHz and 40 MHz for the high-frequency probe. Three dimensional image reconstruction was performed using a modified backprojection formula [16], and subsequent processing of data sets was performed, by discarding negative values and optimal visual adjustments of image intensity values.

After image reconstruction, linear spectral un-mixing was applied to each voxel to specifically detect volumes containing the injected contrast agent. Before un-mixing, images obtained at different wavelengths, were corrected for wavelength-dependent fluctuations in laser power. The light fluence distribution was assumed constant for all wavelengths because of the size of the sample and of the arrangement of the fibers, delivering a homogenous illumination pattern. For each voxel, the multispectral detection method [10] fitted the reconstructed absorbed spectrum within this voxel with the absorption spectra of the expected compounds contained in the sample. Four known spectra were used and corresponded to the hemoglobin (oxygenated and deoxygenated), the contrast agent (measured with the spectrometer), and a constant spectrum for background modeling.

Composite images were formed to present the results of un-mixing algorithm for the injected contrast agents along with an anatomical image of the organ's vascular. The composite images were obtained by merging the un-mixing image with the optoacoustic image obtained at the peak absorption wavelength of the corresponding contrast agent on a dual-channel image. Different color channels were selected for the contrast agent for enhanced visualization purposes, while the single wavelength image was displayed in gray.

2.6 Validation methods

For validation of histo-anatomical information, several optical imaging methods were used: 3D ultramicroscopy imaging, a cryosectioning device and optical microscopy using different staining methods. Due to specific characteristics required by each of the methods, different organ samples had to be selected for 3D ultramicroscopy and cryostat sectioning. 3D Ultramicroscopy validation was performed using a commercial available device (LaVisionBioTec). For enhanced vessel visualization an intravascular injection of 2 nmol Lectin-InvivoTag750 (PerkinElmer) was performed 5 minutes before the animal was sacrificed and the organ was excised. The sample was fixed in PaxGene (PreAnalytiX) as described before [22] and thereafter underwent a chemical procedure of optical clearing according to ref [23]. After dehydration in ascending ethanol series (3 x 70%, 2x 80%, 1 x 90%, 1 x 95%, and 2 x 100% for 30 minutes each, 100% over night) the sample was transferred in a clearing solution of dimethylether (Sigma Aldrich) for 3 days at 4°C. The cleared specimen was scanned using a x0.63 magnification with a x2 objective lens (MVPLAPO 2x, Olympus), achieving an in-plane resolution of 5.1 µm, and 4 µm along the vertical dimension. In order to visualize the specific lectin-InvivoTag750 signals a filter-set with excitation range 740/35 and emission range 795/50 was used. For visualization purposes, the ultramicroscopy data set was inverted, such that the entire vascular volume is visible, and not only the lumen walls stained by Lectin. This solution reveals the renal calyx (marked by "**CA**" in Fig. 2) as well as the vascular patterns (marked by "**VE**"). Secondary validation methods for anatomical correspondence used a Leica CM1950 (Leica Microsystems) cryomicrotome device to generate 20 µm thick slicing planes of the entire sample. For increased resolution and specificity of our validation methods, hematoxylin and eosin (H&E) and CD31 (Zitat) immunostaining for vessel detection was performed on two consecutive thin slices of the kidney for anatomy validation in regions of interest.

#237714 Received 13 Apr 2015; revised 6 Jun 2015; accepted 9 Jun 2015; published 31 Jul 2015

Gold nanorod localization in the kidney excised from mouse *#1* was performed by means of darkfield microscopy. After the optoacoustic scan, the kidneys were stored at −80°C until sliced in a cryotome. Selected representative fresh-frozen 12 μm thick slices through the kidneys were collected and imaged to confirm the distribution of gold nanorods. Darkfield microscopy was performed using a Leica DM 2500 upright microscope mounted with an oil darkfield condenser (NA = 1.2-1.4) and with a 10x oil objective HC PL APO and an x40 HCX PL APO (Leica Microsystems). Pictures were taken using a DFC 360FX color camera (Leica Microsystems).

Validation and localization of the organic dye in the excised kidney of mouse *#2* was performed after optoacoustic measurements by means of fluorescence cryoslicing imaging [24]. The sample was sliced using a cross section step of 100 μm and for each slicing plane photographic images recording the color and fluorescence information were taken by using appropriate filters. Fluorescence excitation was performed using a filter at 740 nm +/– 40 nm on a white light and detection was done using a 785 nm long-pass emission filter.

3. Results and discussion

3.1 Distribution of gold nanorods (AuNR)

Three-dimensional tomographic MSOM data sets were acquired from a kidney excised from a mouse injected with gold nanoparticles. Resulting reconstructed images are shown in Fig. 2 and are compared to ultramicroscopy results. Images correspond to the overlay of an optoacoustic image acquired at a single wavelength, showing the anatomical background, and in yellow the results of an un-mixing algorithm, which captures the absorption spectrum of the injected agent. Figure 2(a), 2(b) depict maximum amplitude projection (MAP) images along the z-axis of reconstructions obtained using the 24 MHz and the 6 MHz transducer array respectively. The yellow overlay corresponds to signals emitted specifically from the gold nanoparticles and reveals an elaborate bio-distribution pattern throughout the images. Both the low frequency and high-frequency images depict a broad distribution of the nanoparticles through more than 60% of the entire volume of the kidney. The low-frequency image shows primarily signals in the thicker vessels, while the higher resolution image – Fig. 2(a) - confirms the presence of gold nanoparticles in smaller micro-vessels sized down to 30 μm. A corresponding ultramicroscopy MAP image (Fig. 2(c)) shows good correspondence of the anatomical information seen on Fig. 2(a), 2(b) from approximately the same kidney area as the one shown on Fig. 2(a), 2(b). The network of thin micro-vessels forming the renal cortex can be clearly registered between the three MAP images. The impact of frequency content on the resolved anatomical structures can be seen on Fig. 2 panel **I** and **II**, where a selected area of the MAP images is presented. The high-frequency image provides a detailed view of the network of vessels and micro-vessels, resolving smaller structures not present on the low frequency data set. The impact of the lower frequency becomes more apparent in the results shown in Fig. 3, however it can be already seen in Fig. 2(e) for example, where the wall thickness of the kidney shows better congruence with the wall appearance in Fig. 2(f), compared to the high frequency image in Fig. 2(d).

#237714 Received 13 Apr 2015; revised 6 Jun 2015; accepted 9 Jun 2015; published 31 Jul 2015

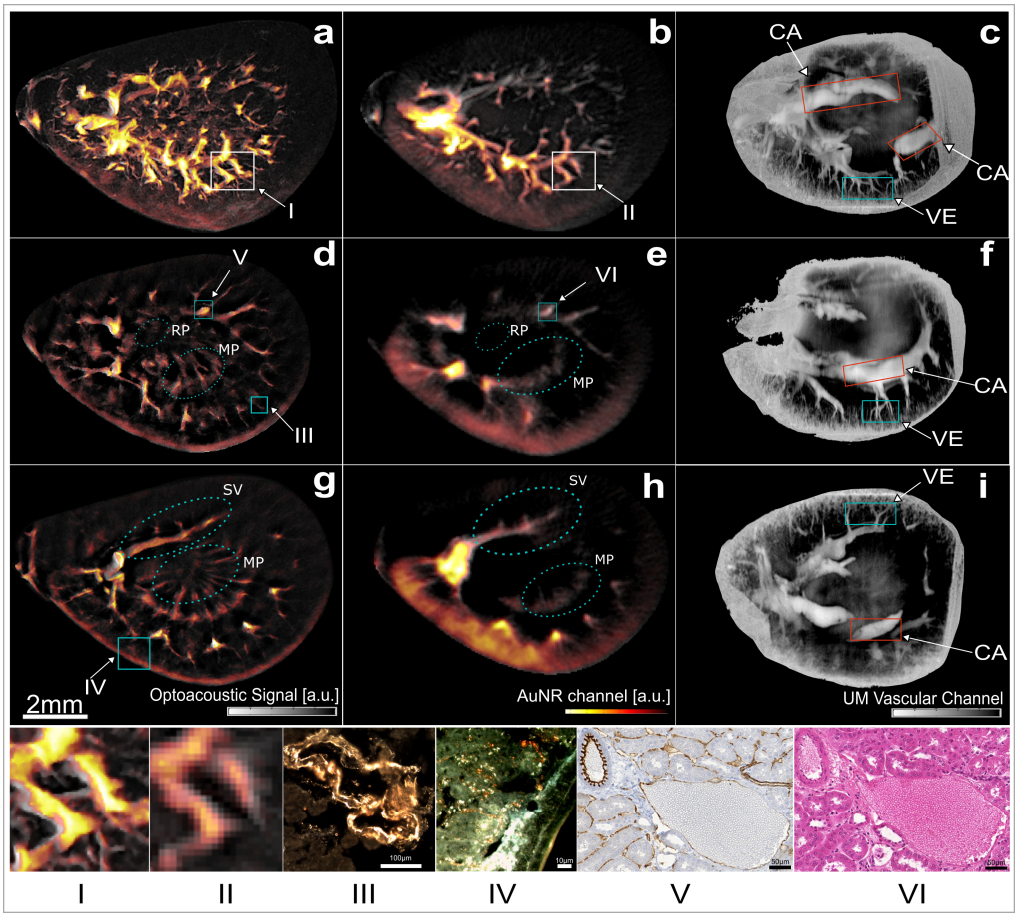

Fig. 2. Ultra-wideband Multispectral Optoacoustic Mesoscopy of Gold Nanorod detection in murine kidney – mouse *#1*. Spectral un-mixed images for the gold nanorods are overlaid in yellow on a single wavelength image acquired at 765 nm (gray). (First row) Maximum amplitude projection (MAP) optoacoustic images along the z-axis respectively for **a,** the 24-MHz array and **b,** the 6-MHz array; **c,** MAP ultramicroscopy image of the optically cleared sample. (Second row) Optoacoustic images corresponding to the in-plane slice at z = 0.7 mm for **d,** the 24 MHz array and **e,** the 6 MHz array; **f,** ultramicroscopy slice corresponding to a similar plane. (Third row) Optoacoustic images corresponding to the in-plane slice at z = 1.4 mm for **g,** the 24 MHz array and **h** the 6 MHz array. **i,** ultramicroscopy image approximately corresponding plane. (Scale bar: 2 mm.) (Panel) (**I & II**) Magnified view of an optoacoustic image region at (**I**) high-frequency and at (**II**) low-frequency; Dark-field Microscopy images corresponding to **(III)** a blood vessel (scale bar 100 µm) and to **(IV)** a region in the renal cortex (scale bar 10 µm); (**V**) DAB and CD31 staining of an artery and a vein (scale bar 50 µm), and **(VI)** H&E Staining of the same region (scale bar 50 µm). The boxes on the images (**a,b,d,e,g**) indicate the approximate location of the features shown on the panel images. The color boxes in (**c,f,i**) delineate regions where **CA** – the calyx, **VE** – vessels, can be visualized. Legend: **RP**– Renal Pelvis; **SV** – Segmental Vessel; **MP** – Medullary Pyramid;

Figure 2(d) displays a cross-sectional plane around the medial plane of the kidney generated using the high-frequency transducer. Enhanced resolution and structural delineation reveals several anatomical structures like the medullary pyramid or the microvasculature forming the renal cortex, which are not resolved by the low-frequency transducer (Fig. 2(e)). In the low-frequency image (Fig. 2(e)), agent detection in the renal cortex is highlighted in yellow due to the dense microvasculature in this area. The presence of gold nanoparticles in vessels larger than capillaries, such as interlobular and arcuate vessels, is visible in the high-frequency image, where these specific structures are resolved. Figure 2(f) shows an ultramicroscopy planar view of a cross section of the kidney, corresponding to the closest

#237714 Received 13 Apr 2015; revised 6 Jun 2015; accepted 9 Jun 2015; published 31 Jul 2015

visually selected corresponding plane. The image validates the anatomical information obtained using the broadband detection system used during the optoacoustic acquisition, but does not contain any functional information regarding the nanoparticle distribution, implying a MSOM contrast superiority. Figure 2 panel **III** shows the result of a dark field microscopy scan performed on the region of interest marked by box **III** shown on Fig. 2(d), confirming the presence of the nanoparticles in the vascular network. Moreover, Fig. 2 panels **V** and **VI** present CD31 and H&E stained slices obtained from a region of interest in a 2D slice, showing the kidney morphology and microvascular pattern.

Figure 2(g) shows the result of a second cross-section through the kidney, where the high-frequency optoacoustic scan reveals several anatomical structures, i.e. the segmental vessel, the microvasculature forming the renal pyramids and the empty renal pelvis. The anatomical image is complemented by the molecular information, depicted in the superimposed yellow colormap, showing a different pattern of nanoparticle distribution compared to Fig. 2(d). The corresponding low-frequency result of the same cross-section as in Fig. 2(g) is presented in Fig. 2(h). Figure 2 – panel **IV** is a dark-field microscopy image that validates the presence of gold nanoparticle on a region of the renal cortex indicated on Fig. 2(g) by box 1. This result confirms the distribution of gold nanorods in the fine structures of the renal cortex. Figure 2(i), the corresponding ultra-microscopy image confirms the MSOM results. Interestingly, the anatomical structures revealed by ultramicroscopy are better captured by the low-resolution (low frequency band) MSOM image in Fig. 2(h).

3.2 Ultra-wideband optoacoustic imaging of renal clearance of IRDye 800CW

To elucidate whether MSOM could follow different distribution patterns based on optical labels we performed multispectral acquisitions on kidneys from mice injected with the fluorescence dye IRDye 800CW. A secondary, but equally important goal of the study, was to reveal whether common fluorochromes could be captured by MSOM, in analogy to SPIM or OPT. Broadband imaging results are shown in Fig. 3. The IRDye 800CW is known to clear through the kidney within minutes after injection, by accumulating in the renal pelvis before excretion [20]. Figure 3(a) depicts a high-frequency 2D cross sectional optoacoustic image at single optical wavelength (774 nm). The green overlay on Fig. 3(a) indicates the result of un-mixing the absorption spectrum of the organic dye based on the lower frequency contributions. Due to the larger size of the fluorescence lesion, there are no significant high-frequency components generated. In other words, the high-frequency images could not capture any fluorescence bio-distribution, since the fluorescence area established in the kidney emits only low frequency ultrasound signals (in the 500 kHz – 2 MHz region) not captured by the high-frequency detector. Correspondingly no high-frequency un-mixed signals are shown herein. This combination of broadband MSOM spectral data validates our original hypothesis that accurate imaging requires 2B-MSOM. This system shows a threshold detection of a volume as small as 2% of the total volume of the biological sample. Figure 3(b) is a corresponding cryoslice image. The color image is a photograph of a kidney cross-section, obtained by physically slicing though the kidney and placing it under a camera. The green signal shown on Fig. 3(b) is the superposition of fluorescence as seen through a fluorescence filter, showcasing the presence of the fluorescence dye solely in the renal pelvis of the kidney. Figure 3(b) is an invasive image that validates the finding in Fig. 3(a) and confirms that it is only through broadband detection that a complete picture of the underlying bio-distribution is possible by MSOM. This result strengthens the hypothesis that multi-scale detection is crucial for accurate bio-distribution analysis, especially if target-sizes change over time, a common scenario for many injected agents.

Figure 3(c) shows MAP optoacoustic images, relying on contrast generated by absorbing hemoglobin obtained at an excitation wavelength of 774nm. The image depicts a lateral view of the kidney, where a clear visualization of vascular networks is possible. Figure 3(d) shows a side view MAP optoacoustic image of the volumetric reconstruction obtained using the low-frequency transducer. Several anatomical structures can be localized in the low and high frequency MAP images, but a more detailed visualization of endogenous contrast is possible

#237714 Received 13 Apr 2015; revised 6 Jun 2015; accepted 9 Jun 2015; published 31 Jul 2015

in the higher resolution image. For anatomical validation purposes a supplementary fresh sample was sliced in thin slices (20 µm), and the MAP image of the reconstructed volume is presented in Fig. 3(e). The difference between the exact shapes on the optoacoustic and cryosection MAP images can be attributed to orientation differences. Due to the difference in aperture size of the two transducers shown, the field of view of the high-frequency transducer is somewhat smaller, as indicated by the dotted yellow line in Fig. 3(d), 3(e).

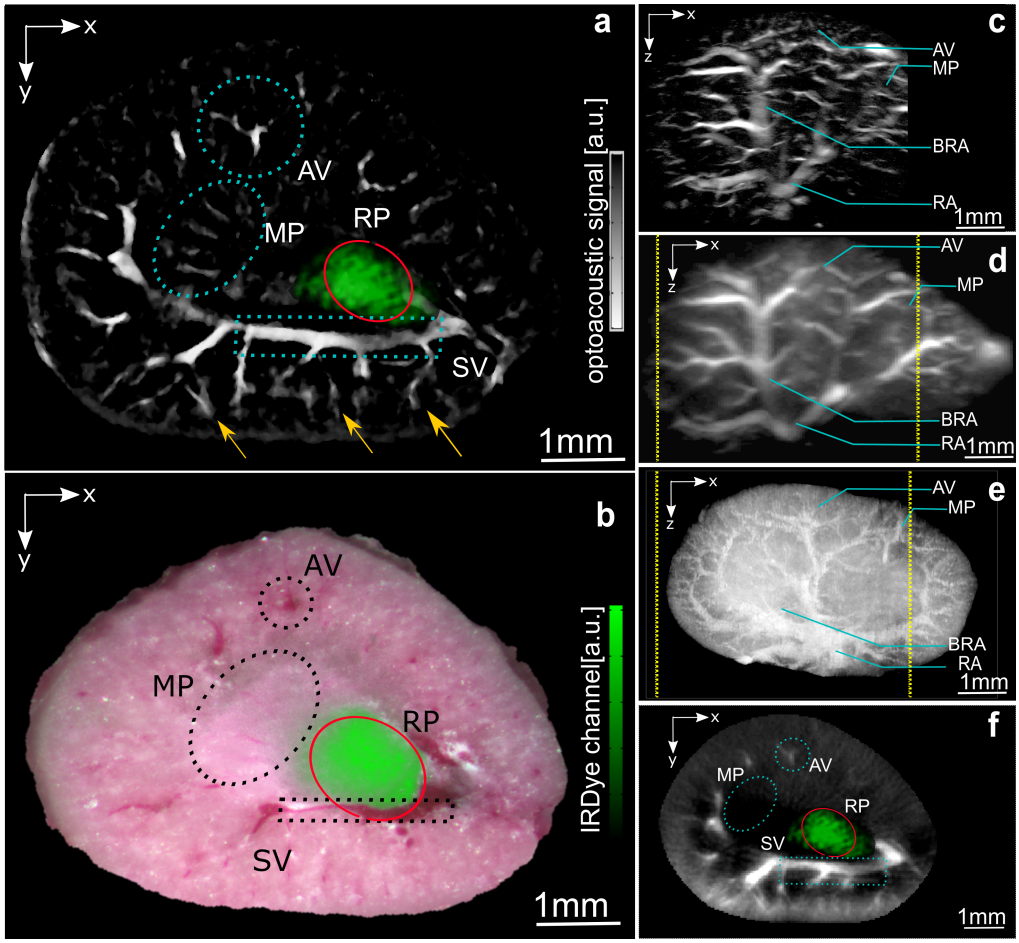

Fig. 3. Ultra-wideband Multispectral Optoacoustic Mesoscopy of Organic Dye in murine kidney - mouse *#2*. The optoacoustic images correspond to the peak absorption wavelength of the injected dye (774nm), and are displayed in a gray scale colormap. **a,** IRDye 800CW detection (green) overlay on a high-frequency 2D plane; the agent detection was based on the scan performed using the low-frequency transducer. **b,** Corresponding cryosection photographs and fluorescence signal detection of the agent (green); **c,** High-frequency, **d,** low frequency and **e,** Cryosection MAP image along y-axis; **f,** 2D low-frequency plane corresponding to the plane presented in **a**; **AV** – Arcuate vein; **MP** – Medullary Pyramid; **BRA** – Branching of Renal Artery; **RA** – Renal Artery.

3.3 Frequency dependent compartmental study of agent distribution

The elaborate patterns revealed by MSOM allow the understanding of distribution patterns in different sub-structures of the kidney. This is an important determinant of the characteristics of different agent studies. One elaborate feature of the MSOM signal is that different substructures generate different frequencies depending on their size. We therefore undertook a study where we looked in a frequency dependent manner on the relative contributions of the

#237714 Received 13 Apr 2015; revised 6 Jun 2015; accepted 9 Jun 2015; published 31 Jul 2015

agents examined. To achieve this we defined 3x3x3 voxel sub-volumes selected within 4 different anatomical regions in the reconstructed kidneys. Figure 4 summarizes the analysis and relative contributions for the AuNR and the IRDye 800CW fluorescent dye in the four selected compartments, i.e. the renal cortex, the renal pelvis, in macrovessels and in microvessels. Figure 4(a) depicts the results of the analysis for the high-frequency component (2 - 40 MHz). Signal generated by AuNR is majorly detected in the macro and microvasculature, with higher preference for smaller vessels. The nanoparticles do not exhibit significant contributions from the renal cortex, or the renal pelvis. Correspondingly, a small fraction of the IRDye is found in the vasculature. Finally, Fig. 4(a) also shows the compartmental contributions of the total hemoglobin, representing the blood component in the volume of interest, and shows good agreement with physiological expectations of blood pool presence in the renal vasculature. Figure 4(b) correspondingly shows the analysis for low frequency components (500 kHz – 12 MHz). In this view, AuNR presence in the renal cortex as well as in both macro- and microscopic blood vessels is shown. The analysis also shows the lack of AuNR retention in the renal pelvis. Conversely a strong contribution from the IRDye is observed in the renal pelvis. Hemoglobin is similarly confirmed in the vasculature. Figure 4(c), 4(d) show the regions of interest selected in the high-frequency analysis and Fig. 4(e), 4(f) show the regions of interest selected in the low-frequency analysis. The results herein clearly show that the implementation frequency of an MSOM system will affect the quantification of the technique; assigning different values to different compartments. This conclusion further justifies the selection of ultra-wideband MSOM for accurate quantification of different distribution patterns.

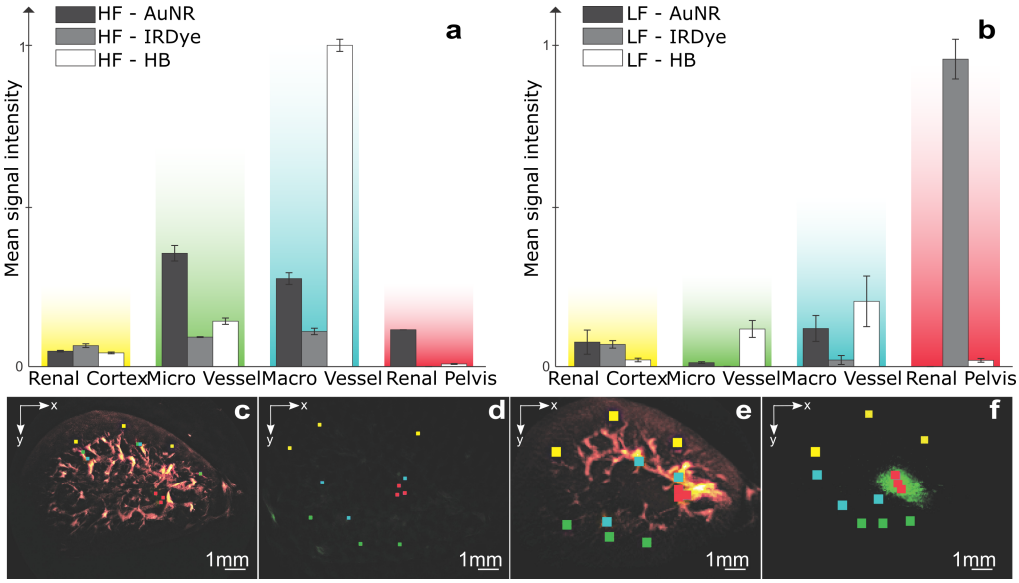

Fig. 4. Compartmental study of agent distribution for different frequency bands. Mean signal amplitude for 4 regions of interest selected in **a,** high frequency and **b,** low-frequency data sets; **c,** and **d,** Regions of interest selected for the high frequency analysis; **e,** and **f,** Regions selected for the low frequency analysis. Seed points for region selection overlaid on the color images: red – Renal Pelvis; yellow – renal cortex; blue – macro-vasculature; green – micro-vasculature.

2B-MSOM was shown also capable of retrieving elaborate tissue anatomy. High-frequency 2B-MSOM images resolved small blood vessels such as the arcuate and interlobular vessels (Fig. 3(a) – yellow arrows), which are not visible in lower frequencies (Fig. 3(f)). The ability of optoacoustic methods to resolve blood vessels has been well demonstrated [25]. Interestingly however, the information contained in the lower frequency part of the 2B-MSOM data set provided insights to larger anatomical structures that would

#237714 Received 13 Apr 2015; revised 6 Jun 2015; accepted 9 Jun 2015; published 31 Jul 2015

have been missed by a narrower band implementation. For example, larger structures such as large vessels, the kidney wall or distributed pools of fluorescence accumulation can only be seen in the lower-frequency band as seen in Fig. 2(e) or Fig. 3(a).

Compared to SPIM or OPT, 2B-MSOM could enable imaging of opaque specimen and/or large specimen (in the 1-5 mm range) without the need for chemical treatment. To understand the relevance to SPIM, 2B-MSOM results were compared herein to ultramicroscopy images, effectively implementing SPIM of cleared specimen. The comparison between optoacoustic images on untreated specimen and SPIM images of chemically cleared specimen showcased a congruence of anatomical (absorption) intrinsic tissue contrast. Moreover, 2B-MSOM could resolve not only fluorochromes but also nanoparticles. In addition, although ex-vivo imaging has shown so far possible, a next step would be to enable the 2B-MSOM system for in-vivo imaging, further improving the application field of this method. Regardless, basic features of the 2B-MSOM ability demonstrated herein, herald a potent outlook.

Compared to previous optoacoustic mesoscopy implementations, 2B-MSOM demonstrated significant imaging improvements. Single detector implementation at 15 MHz [10] only captured a ~7 MHz spectral band (11-18 MHz) at a significantly lower spatial-frequency range. The overall imaging ability of this original 15 MHz implementation suffered from insufficient aperture along the coronal dimension, lower resolution than the 2B-MSOM system and formed only single-plane two-dimensional images. It was the particular implementation of an extended frequency range (0.5 - 40 MHz) and the use of a high-spatial-frequency pattern employing 128-detectors in parallel, which enabled true three-dimensional operation, yielding accurate imaging performance. The use of multiple ultrasonic transducers to record a broadband spectrum has been previously considered in single-element scan investigations that aimed at comparing the contrast and resolution improvements at single-wavelength optical excitation [26]. Therefore, the relation between bandwidth and dye bio-distribution could not be established in these studies. Moreover, it was not possible to relate bandwidth to high-spatial sampling, three-dimensional tomographic images. Other detection technologies using optical intereferometry [27] benefit from a large detection bandwidth [28]. These implementations are limited to planar raster-scan geometries possibly introducing limited view artifacts. Compared to previously reported raster scan approaches [29–31], 2B-MSOM demonstrated high and homogeneous in-plane resolution, three-dimensional imaging capacity, the ability to resolve contrast beyond blood vessels and high-frequency structures and the ability to resolve nanoparticle and fluorescence bio-distribution at resolutions better than 30 μm through at least 3 mm of tissues. No optoacoustic method has achieved such performance so far.

The investigation herein considered imaging of agents of varying molecular weight, i.e. low molecular weight organic compounds and gold nanoparticles exhibiting markedly different bio-distribution patterns but near-infrared absorption, to enable low light attenuation in tissue. Specific detection of the injected particles was achieved using spectral un-mixing [32], which identified the injected agents based on their absorption spectrum; revealing functional information, which was then superimposed on anatomical/vascular features of the kidney. The un-mixing method accurately resolved the different patterns of the photo-absorbing agents used. High-spatial-resolution patterns were revealed for the gold particles, corresponding to high ultrasound frequencies and low spatial resolution (larger area) patterns for fluorochrome accumulation, corresponding to lower ultrasound frequency. An important factor in biomarker detection is the number of wavelengths used for optical excitation. Based on the absorption spectra of the injected dye, we choose a selection of 5 wavelengths for each of the injected probes: for AuNR – 715nm, 740nm, 765nm, 790nm, 815nm; and for IRDye – 725nm, 750nm, 774nm, 800nm, 825nm; this selection can discriminate in an optimal and stable manner the three components that we have assumed to account for the optoacoustic signal: oxygenated hemoglobin, deoxygenated hemoglobin and the injected agent. A larger variety of wavelengths could be selected for allowing un-mixing of multiple agents.

Another important factor accounting for image quality and for the detection of the injected agent especially in small and directive structures as blood vessels is the number of projections

#237714 Received 13 Apr 2015; revised 6 Jun 2015; accepted 9 Jun 2015; published 31 Jul 2015

used during the acquisition. Typical acquisition scans acquired 9060 laser shots*128 elements = 1.159.680 projections over 180° degrees and 9 mm translation range for the 24 MHz scan and 2700 laser shots *128 elements = 345.600 projections for the 6 MHz. The high spatial frequency sampling herein was necessary to offer high-quality images of structural, functional and molecular information. Reducing the number of projections could reduce the acquisition time but also increase image noise and artifacts. One approach to improve imaging performance in limited spatial sampling scenarios is to utilize improved reconstruction schemes that model the spatio-temporal response of the detector and of the geometry implemented and in particular account for the acoustic lens of the detector. Such reconstruction schemes have been shown to provide better image quality with less projections [33]. In addition to reducing the number of projections, careful consideration of the transducer's spatio-temporal response during the image reconstruction could enable combining the optoacoustic signals generated by the two transducer arrays in a single image comprising the information from the extended frequency range, and could therefore allow direct comparison of the contrast agent distribution in a broad range of structure sizes. For the acquisition duration, a limitation of the current study was imposed by the low repetition rate (10 Hz) of the pulsed laser employed for optical excitation, which yielded acquisition times of ~15 minutes per wavelength for the high-frequency transducer and ~5 minutes for the low-frequency transducer. Using 100 Hz lasers instead could accelerate acquisition to less than two minutes of imaging time; plus the time required for specimen or system rotation and translation.

In the context of kidney imaging, several studies concerning renal vasculature, filtration and glomeruli count have revealed a relation between kidney pathology and diseases of the cardiovascular system [34]. Kidney imaging has been analyzed for an accurate assessment of the arrangement of intra-renal veins with regard to the collecting system [35]. Furthermore, imaging of the urological system can be used for disease progression in renal carcinoma, fibrosis [36] or nephrocalcinosis, making kidney imaging a tool for prevention and diagnosis. Even though the presented approach demonstrated kidney features ex vivo, renal structures can be visualized at high resolution in a fraction of the time that would be required for histological approaches. Moreover, both label-free and dye/nanoparticle contrast was demonstrated and differentiated. In this manner, the need for extensive tissue-preparation is eliminated, allowing the study of freshly excised specimens. The need of using complex reconstruction algorithms to compensate for frequent defects present in histological slices, e.g. holes, folds and tears, is also avoided [37].

4. Conclusion

In summary, the results presented herein show that the use of a rich, five-dimensional data set is essential for accurate MSOM implementation. 2B-MSOM was found capable of retrieving fluorochromes and photo-absorbing particles over a wide range of structural complexity through a thick and opaque biological sample. 2B-MSOM resolved both anatomical information generated by the absorption of hemoglobin present in tissues as well as physiological information, i.e. information on kidney clearance patterns; the result of injected agents. This first implementation of 2B-MSOM, using multi-angle projection data, exhibited imaging resolution of better than 30 μm through at least 3 mm of opaque specimen. Although 2B-MSOM is in a much earlier development stage than SPIM, the resolution that 2B-MSOM achieves is possibly at a better analogy to the resolution achieved in SPIM. SPIM can offer resolution of the order of 6 μm but requires specimen no larger than 200-300 μm, assuming untreated specimen to ensure transparency, i.e. a depth/resolution ratio of 50 (300:6). Correspondingly, 2B-MSOM showed a depth/resolution ratio of 100 (3000:30). While these numbers are understandably approximate and largely depend on the specific samples imaged, they indicate that 2B-MSOM has an equal or better scaling capacity than SPIM. They also show that SPIM and 2B-MSOM could be complementary, in particular when considering in-vivo applications of specimen of varying sizes. With the current configuration, in-vivo optoacoustic imaging of endogenous contrast in other specimen such as small animals, fish,

#237714 Received 13 Apr 2015; revised 6 Jun 2015; accepted 9 Jun 2015; published 31 Jul 2015

or rodent extremities could be envisioned in order to provide anatomical information. Moreover, detection of extrinsic contrast or the expression of reporter genes could reveal physiological or cellular and molecular parameters. Next steps therefore would include the acceleration of imaging through the utilization of faster lasers; in order to provide for a high-throughput modality and allow in-vivo imaging as well.

Acknowledgments

The authors would like to thank N. Burton and S. Gottschalk for helpful discussions. We would also like to thank S. Glasl and U. Klemm for their technical support and the laboratory mouse handling. We would like to thank T. Cosmatu for graphical design. The research leading to these results has received funding from the European Union (European Research Council, ERC-2008-AdG) under grant agreement no. 233161, MSOT, and by the DFG Cluster of Excellence "Nanosystems Initiative Munich (NIM)".